communications earth & environment

Article

A Nature Portfolio journal

https://doi.org/10.1038/s43247-026-03379-1

Stability and distribution of dense hydrous magnesium silicates in the mantle transition zone under low water activity conditions

Yunke Song [1,2,3], Xinzhuan Guo [4] ✉, Kuan Zhai [1], Wei Guo[5] & Takashi Yoshino [6]

Water plays a central role in controlling the physical and chemical properties of Earth's deep interior. It remains uncertain how water is stored in subducting slabs within the mantle transition zone, between depths of about 410 and 660 kilometers, and whether dense hydrous magnesium silicates act as major water carriers to greater depths. Here we report high-pressure and high-temperature laboratory experiments on the Mg-Si-H system at pressures of 16 and 21.5 GPa and a temperature of 1400 K to evaluate hydrous phase stability under transition zone conditions. We find that when bulk water content is below 1.22 wt%, H_2O is predominantly incorporated into wadsleyite and ringwoodite rather than forming dense hydrous magnesium silicates. Because estimated water contents in subducted oceanic slabs are typically lower than one weight percent, formation of these silicates is unlikely, suggesting that the mantle transition zone may restrict large scale water transport into the lower mantle.

Water plays a pivotal role in shaping the physicochemical properties, structure, and dynamics of the Earth's deep interior, as documented by previous studies[1–5]. Consequently, numerous investigations have been carried out to examine the distribution of water within the deep mantle, including phase equilibrium experiments and theoretical calculations. It is widely accepted that dense hydrous magnesium silicates (DHMSs) in the cold slab play a crucial role in transporting water into the Earth's interior. Water is transported by phase A following the serpentine breakdown at 7 GPa, and subsequently by other high-pressure DHMSs[6–8]. The currently reported highest-pressure form of these DHMSs, phase H, is stable at depths far deeper than 1250 km. The stability of phase H may be further expanded to the core-mantle boundary on the dissolution of the δ-AlOOH component in the structure, even at the normal mantle geotherm[9–11]. However, most previous experimental studies on the stability of DHMSs have been conducted under water-saturated conditions, while water activity plays an indispensable role in the stability of hydrous minerals.

The subducting oceanic slab typically comprises three petrological layers (sediment, basalt, and depleted peridotite). According to the phase equilibrium experiments in sediment and mid-ocean ridge basalt (MORB) compositions, the bulk water content in the sediment retains less than 0.5 wt % H_2O at pressures higher than 12 GPa, and the MORB almost dries out after the breakdown of lawsonite at pressures higher than 10 GPa[12]. Recent experiments suggest that Al-bearing stishovite can incorporate >1 wt% H_2O, but their water content is highly temperature-dependent[13,14]. Under the low temperature characteristic of subduction zones, the $CaCl_2$-type SiO_2 cannot form. For the peridotite layer, although complete serpentinization of peridotite could theoretically introduce up to ~13 wt% H_2O into the slab[6], antigorite breakdown to enstatite, phase A and H_2O at ~7 GPa, via the reaction 5Antigorite = Phase A + 8Enstatite + 7H_2O, yields the maximum bulk water content retained in the slab is 4.3 wt%. However, hydration levels may be much lower in nature system. Seismic studies[15] indicate serpentinization of only 19 vol% in the peridotite layer, which has a thickness of 24 ± 5 km; this corresponds to a bulk water content of 2 wt%. After further breakdown of serpentine to phase A, the water content that can be retained in the slab drops to only 0.82 wt%. Furthermore, studies have shown that with 20% serpentinization, the resulting density contrast is insufficient to

[1]Key Laboratory of High-temperature and High-pressure Study of the Earth's Interior, Institute of Geochemistry, Chinese Academy of Sciences, Guiyang, China. [2]University of Chinese Academy of Sciences, Beijing, China. [3]Bayerisches Geoinstitut, University of Bayreuth, Bayreuth, Germany. [4]State Key Laboratory of Critical Mineral Research and Exploration, Institute of Geochemistry, Chinese Academy of Sciences, Guiyang, China. [5]State Key Laboratory of Geomicrobiology and Environmental Changes, School of Earth Sciences, China University of Geosciences (Wuhan), Wuhan, China. [6]Institute for Planetary Materials, Okayama University, Misasa, Japan. ✉e-mail: gxzhuan@mail.gyig.ac.cn

overcome slab negative buoyancy and initiate convective overturn[16]. In addition, our previous results have demonstrated that water activity is a key parameter controlling the stability of hydrous minerals. Brucite[17] and superhydrous phase B[18] have shown that the onset temperatures of partial dehydration under low water activity conditions are 50–200 K lower than those under water-saturated conditions. This suggests that the stability of hydrous minerals is not only controlled by temperature and pressure but is also related to water activity. In subducted slabs with low bulk water contents (e.g., <1 wt%), the transformation of olivine to wadsleyite (Wd) and ringwoodite (Rw) provides an efficient mechanism for redistributing water. Wd and Rw are known to accommodate more than 2 wt% of H_2O, although reported solubilities vary widely depending on pressure, temperature, composition[19–23]. Ongoing debates remain regarding the maximum H_2O contents achievable under natural mantle conditions.

If water preferentially enters Wd and Rw, DHMSs become negligible and cannot serve as major water carriers in the mantle transition zone. Although there are a large number of phase equilibrium studies in the MgO-SiO_2-H_2O (MSH) system with pyrolite composition at transition zone depths, experiments with initial H_2O content <2 wt% have seldom been explored except for speculation[24]. It is essential to determine the phase relations of the peridotite with low water contents for a better understanding of water distribution in the mantle transition zone (MTZ). Here we investigate the phase relations in the MSH system with various water contents (from 0.1 to 5 wt%) at pressures of 16 and 21.5 GPa and 1400 K to examine whether DHMSs can or not serve as the water carriers in the MTZ with various bulk water contents.

Results and discussion

High-pressure experiments

Experimental assembly design and methods of analysis are described in the Method. At 16 GPa and 1400 K, the run products with 0.1 wt% bulk water content include Wd and high-pressure clinoenstatite (En). With increasing bulk water content to 1.6 wt%, phase E appears, and its volume fraction increases with initial bulk water content in the starting materials (Fig. 1). The electron backscatter diffraction (EBSD) technique reveals that each phase is homogeneously distributed despite some grains being lost during the polishing process (Fig. 2a, b). At 21.5 GPa and 1400 K, the run products with 1 wt% bulk water content are akimotoite and Rw. When the bulk water contents increase to 1.6, 3, and 5 wt%, the phase assemblages changes from Rw + akimotoite (Ak) + superhydrous phase B (SuB), through Ak + SuB + stishovite (St) to SuB + St (Fig. 2c, d), which are consistent with results from previous experimental studies with 3–5 wt% water content (Fig.1b). At higher Mg/Si = 2, the run product contains more Rw. On the contrary, when Mg/Si is close to 1, there will be excess phase D at higher bulk water contents[7,25,26]. In addition, the water contents of Rw and Wd in the experimental products were directly determined by secondary ion mass spectrometry (NanoSIMS). We used synthetic hydrous Rw as the reference standard, and its water content was calibrated by Fourier-transform infrared spectroscopy. Detailed experimental conditions and results are listed in Table 1 and Supplementary Table 1.

Mass balance calculations

The mass balance calculation is an essential method that has been frequently used to evaluate the stability region of the hydrous phase as a function of water content[24,27] and is therefore ideal for evaluating the validity of the present experimental results. We constructed the phase proportion diagram for the MSH system with Mg/Si = 1.4 as a function of total H_2O content at 16 and 21.5 GPa and 1400 K (Fig. 1). Our results unequivocally demonstrate that water preferentially partitions into Wd and Rw instead of DHMSs. In this case, we adopt the maximum water solubility of 2.42 wt% for Wd and 2.57 wt % for Rw, which we directly measured the H_2O contents of Wd and Rw using Nano-SIMS, and the corresponding values are reported in Supplementary Table 1. We set these values as the upper limits of water contents in Wd and Rw. The partition coefficients of H_2O between Wd and En are 3.8, and between Rw and akimotoite are 21[27] to estimate the water contents of En and Ak, respectively. We neglect the water content of St because the system is Al-free. In Al-free systems, the water content in St is lower than 300 ppm, which is negligible compared to SuB (>7 wt%)[28], allowing us to reasonably disregard its contribution to the overall water content in the system. The detailed methodology of mass balance calculation is in Supplementary Discussion.

At 16 GPa, within the Wd stability field, the system consists of Wd and En at the lowest bulk H_2O content (Fig. 1a). With Mg/Si = 1.4, their volume fractions are 43.8% and 56.2%. The maximum H_2O content in this system is 1.22 wt%; exceeding this threshold leads to the appearance of phase E. As H_2O content increases, volume fraction of phase E increases while Wd decreases, disappearing entirely at 5.0 wt% H_2O. At 21.5 GPa, in the Rw stability field, the sample shows an assemblage of Rw and akimotoite at low bulk H_2O content (Fig. 1b). To satisfy Mg/Si = 1.4, their volume fractions are 47.7 vol% and 52.3 vol%, with a maximum total H_2O content of 1.30 wt%. Exceeding this value results in the formation of SuB, reducing Rw content. The equilibrium assemblage consists of Rw, akimotoite, and SuB. When SuB reaches 32.3 vol%, Rw disappears, and total H_2O content reaches 2.14%. Beyond 2.14 wt% H_2O, stishovite appears, and akimotoite reduces. At 4.76 wt% H_2O, stishovite reaches 23.4 vol%, and akimotoite disappears. If

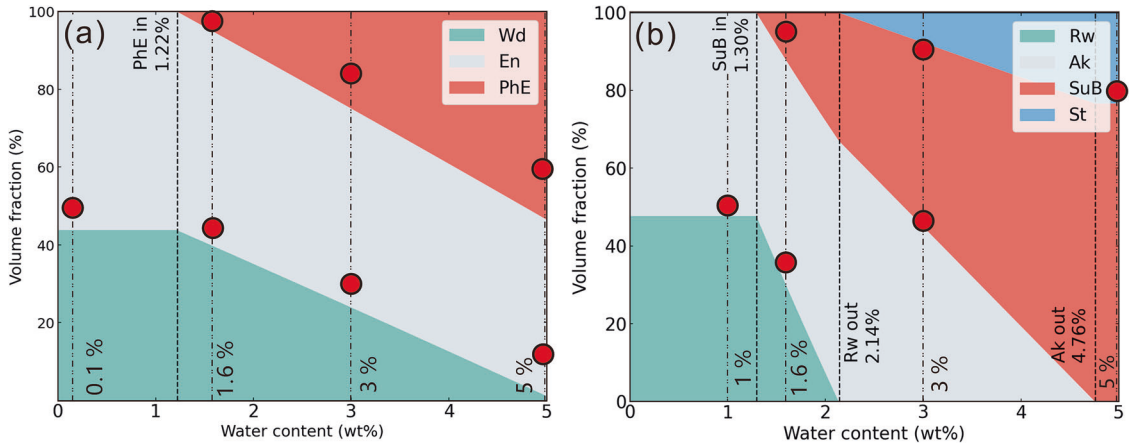

Fig. 1 | The mass balance calculation of the phase volumes in low water content conditions. The red dots represent experimental results. **a** 16 GPa, phE: $Mg_{2.3}Si_{1.25}H_{2.4}O_6$, density and max water content of each phase. Wd, wadsleyite (3.5 g/cm^3, 2.5 wt% H_2O), En, clinoenstatite (3.28 g/cm^3, 0.12 wt% H_2O), phase E (2.92 g/cm^3). The partition coefficient $D_{Wd/En}$ = 3.8 (Detail calculation setting and data source in Supplementary Discussion). **b** 21.5 GPa, superhydrous phase B: $Mg_{10}Si_3H_4O_{18}$, ringwoodite (3.9 g/cm^3, 2.8 wt% H_2O), akimotoite (3.81 g/cm^3, 0.133 wt% H_2O), superhydrous phase B (3.3 g/cm^3), stishovite (4.35 g/cm, 0 wt% H_2O). The partition coefficient $D_{Rw/Ak}$ = 21 (Detailed calculation setting data source in Supplementary Discussion).

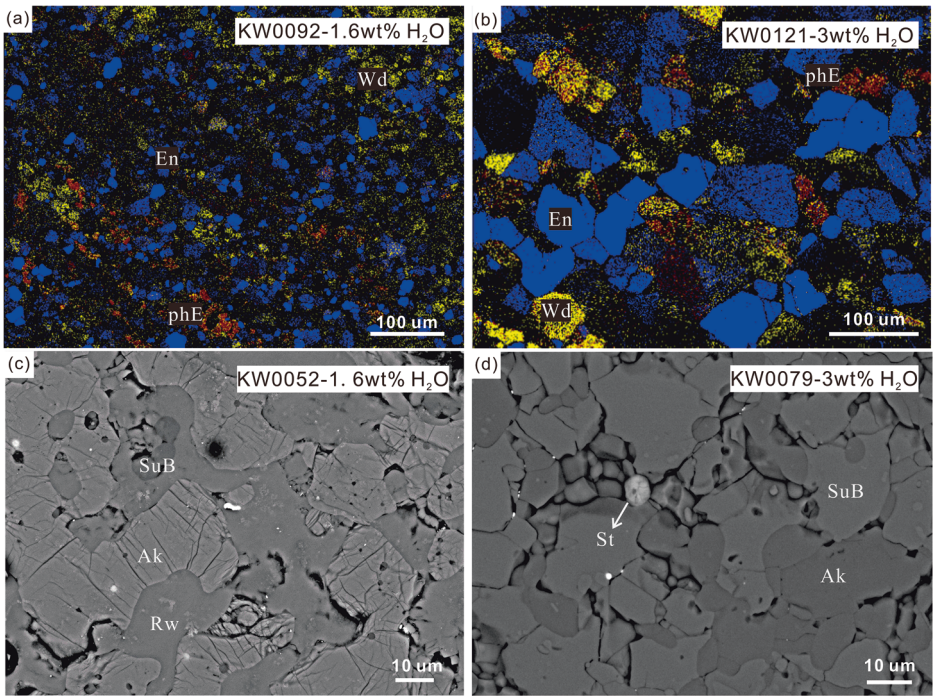

Fig. 2 | Representative BSE and EBSD images of the sample. a KW0092, 16 GPa, 1.6 wt% H_2O. **b** KW0121, 16 GPa, 3 wt%. **c** KW0092, 21.5 GPa, 1.6 wt% H_2O. **d** KW0079, 21.5 GPa, 3 wt% H_2O. Wd wadsleyite, En clinoenstatite, phE phase E, Rw ringwoodite, Ak akimotoite; SuB superhydrous phase B.

Table 1 | Experimental results and mass balance calculation results (16 and 21.5 GPa)

Run no.	Starting material	*P* (GPa)	*T* (K)	Duration (hour)	Run products	Statistics (volume%)	Calculated (volume%)
KW0098	MSH (0.1 wt% H_2O) Mg/Si = 1.4	16	1400	6	Wd+En	Wd (50) En (50)	Wd (43.8) En (56.2)
KW0092	MSH (1.6 wt% H_2O) Mg/Si = 1.4	16	1400	6	Wd+En+phE	Wd (47) En (52) phE (1)	Wd (39.6) En (55.1) phE (5.3)
KW0121	MSH (3 wt% H_2O) Mg/Si = 1.4	16	1400	6	Wd+En+phE	Wd (30) En (55) phE (15)	Wd (23.9) En (51.1) phE (25.0)
KW0135	MSH (5 wt% H_2O) Mg/Si = 1.4	16	1400	6	Wd+En+phE	Wd (15) En (45) phE (40)	Wd (1.1) En (45.3) phE (53.6)
S1376[a]	MSH (3.6 wt% H_2O) Mg/Si = 1.4	15.5	1273		Wd+phE+St		
S1377[a]	MSH (12.2 wt% H_2O) Mg/Si = 1.4	14	1373		En+phE+L		
5k3212	MSH (1 wt% H_2O) Mg/Si = 1.4	21.5	1400	24	Ak+Rw	Rw (50) Ak (50)	Rw (47.7) Ak (52.3)
KW0052	MSH (1.6 wt% H_2O) Mg/Si = 1.4	21.5	1400	6	Rw+Ak+SuB	Rw (35) Ak (60) SuB (5)	Rw (29.8) Ak (57.8) SuB (12.4)
KW0079	MSH (3 wt% H_2O) Mg/Si = 1.4	21.5	1400	6	SuB+Ak+St	SuB(44) Ak (46) St (10)	SuB(44.9) Ak (47.4) St (7.7)
1k2868	MSH (5 wt% H_2O) Mg/Si = 1.4	21.5	1400	12	SuB+St	SuB (80) St (20)	SuB (76.6) St (23.4)
S1387[b]	MSH (3.6 wt% H_2O) Mg/Si = 1.4	20.5	1373		SuB+Rw+St		
E15H04[c]	MSH (15 wt% H_2O) Mg/Si = 1	21.5	1373		SuB+ phase D+L		
F5H22[c]	MSH (5 wt% H_2O) Mg/Si = 2	21.5	1273		SuB+St+(Rw)		

En clinoenstatite, *Wd* wadsleyite, *phE* hydrous phase E, *Ak* akimotoite, *Rw* ringwoodite, *St* stishovite, *SuB* superhydrous phase B, *L* melt.
[a]Data from Komabayashi et al.[8].
[b]Data from Komabayashi and Omori[7].
[c]Data from Ohtani et al.[25].

H_2O content exceeds 4.76 wt%, the equilibrium assemblage stabilizes as stishovite and SuB, with respective volume fractions of 23.4 vol% and 76.6 vol%.

The phase assemblage identification in our experimental results and phase volume fractions align with mass balance calculations, confirming the reliability of the calibration assumptions. When Wd and Rw approach the maximum water solubility, the bulk MSH system in equilibrium contains 1.22 and 1.30 wt% H_2O, respectively, and phase E and superhydrous phase B occur. Therefore, if the water content of the MSH system is lower than 1.22 wt%, all the water will be stored in Wd and Rw. If the water content exceeds 1.22 wt%, DHMSs will eventually occur. This strongly demonstrates that water preferentially enters Wd or Rw, and that DHMSs only form once Wd and Rw become water saturated.

Influences of water activity on the stability of hydrous minerals

Some previous studies have demonstrated that water activity is a critical factor controlling the dehydration reactions of hydrous minerals. For instance, studies on the electrical conductivity of brucite[17] and SuB[18] in open systems reveal that partial dehydration occurs at temperatures 50–200 °C lower under low H_2O activity (a_{H_2O}) conditions compared to water-saturated systems. a_{H_2O} also governs the hydration/dehydration of minerals under high pressures and high temperatures. Taking Rw as an example, water preferentially incorporates into its crystal structure through $2H^+ \leftrightarrow Mg^{2+}$ substitution reaction:

$$Mg_2SiO_4(s) + xH_2O(l) \leftrightarrow Mg_{2-x}H_{2x}SiO_4(s) + xMgO(s)\ (x \le 0.224) \quad (1)$$

The equilibrium constant of this reaction (K_1) is inversely related to a_{H_2O}:

$$K_1 = \frac{a_{Mg_{2-x}H_{2x}SiO_4} \cdot a^x_{MgO}}{a_{Mg_2SiO_4} \cdot a^x_{H_2O}} \propto \frac{1}{a^x_{H_2O}} \quad (2)$$

This relationship highlights that water incorporation into Rw is controlled by an internal solubility equilibrium. A formation of SuB occurs when hydrous Rw approaches its maximum water solubility, following the complex multicomponent reaction:

$$7Mg_2SiO_4(hy, s) + 2H_2O(l) \leftrightarrow Mg_{10}Si_3H_4O_{18}(s) + 4MgSiO_3(s) \quad (3)$$

The corresponding equilibrium constant (K_2) is expressed as:

$$K_2 = \frac{a_{Mg_{10}Si_3H_4O_{18}} \cdot a^4_{MgSiO_3}}{a^7_{Mg_2SiO_4} \cdot a^2_{H_2O,eq}} \propto \frac{1}{a^2_{H_2O,eq}} \quad (4)$$

and is related to the standard Gibbs free energy change:

$$\Delta G^0(T, P) = -RTlnK_2 \quad (5)$$

The instantaneous direction of this reaction is governed by the reaction quotient (Q_2), defined identically to K_2 but based on instantaneous activities:

$$Q_2 = \frac{a_{Mg_{10}Si_3H_4O_{18}} \cdot a^4_{MgSiO_3}}{a^7_{Mg_2SiO_4} \cdot a^2_{H_2O}} \approx \frac{1}{a^2_{H_2O}} \quad (6)$$

The instantaneous Gibbs free energy change is then:

$$\Delta G(T, P) = RTln\frac{Q_2}{K_2} \quad (7)$$

Elevated a_{H_2O} leads to $\frac{1}{a^2_{H_2O}} < \frac{1}{a^2_{H_2O,eq}}$. Consequently, $Q_2 < K_2$ and $\Delta G < 0$, promoting the forward reaction (SuB formation). When a_{H_2O} decreases, Q_2 increases such that $Q_2 > K_2$. This shifts the reaction toward the reverse direction, suppressing the formation of SuB. This contrast highlights fundamental differences in how distinct hydrous phases respond dynamically to water activity.

It is noteworthy that the minimum bulk water content of approximately 1.22 wt% required for DHMS formation, as determined by our calculations, is based on water activity conditions in a pure H_2O system, whereas in MTZ conditions, the water activity in a mixed H_2O–CO_2 fluid is lower than in a pure H_2O system[29,30]. Experimental and theoretical studies have demonstrated that CO_2 acts as a diluent, decreasing the chemical potential and activity of H_2O[31]. This reduction in a_{H_2O} directly limits the formation of DHMSs. In peridotite-buffered experiments, highly non-ideal mixing between H_2O and CO_2 further amplifies the reduction in water activity[32,33]. Moreover, under high pressure, when melt and water are immiscible, the a_{H_2O} in the hydrous melt is greatly reduced. Therefore, if the effect of CO_2 on a_{H_2O} is considered, the stability and water storage capacity of hydrous minerals in the mantle would be considerably overestimated. The effective bulk H_2O threshold is expected to be higher in natural systems.

It should be noted that the lower limit bulk H_2O threshold for DHMS formation derived here is not itself a thermodynamic variable but instead reflects a saturation-controlled constraint. Its numerical value is sensitive to the maximum H_2O storage capacities of Wd and Rw under the investigated pressure and temperature conditions. When the system's composition becomes more complex, the volume fractions of Wd and Rw remain largely unaffected. The presence or absence of other phases has no substantial effect on our results. Furthermore, if Wd and Rw contain certain amounts of elements like iron and aluminum, the impact on their maximum water storage capacities is limited. Therefore, this bulk water content threshold remains highly applicable to the composition of real slabs[22,23]. We emphasize that this critical point is not expected to be invariant. In regions characterized by localized thermal anomalies or in subducting slabs with highly heterogeneous bulk compositions, temperature-dependent variations in the maximum water capacities of Wd and Rw may lead to shifts in the critical threshold for DHMS formation.

The threshold and phase-equilibrium results obtained in our study provide quantitative constraints on the bulk water contents under which subducting slabs are able to transport water to greater depths in the mantle in the form of stable DHMSs. Specifically, when the bulk water content is below the critical threshold, water is predominantly incorporated as hydrogen defects[19] in nominally anhydrous minerals rather than phase-controlled water storage. In this regime, the storage capacity is limited and highly sensitive to temperature and water activity, making water more prone to redistribution or release within the shallow mantle to transition-zone depths. In contrast, once the bulk water content exceeds the threshold and hydrous phases such as DHMSs become stable, aH_2O rises, and the system reaches conditions where water storage shifts from a defect-controlled mechanism to phase-controlled storage, substantially enhancing the efficiency of solid-state water retention and the potential for deep transport under high-pressure conditions. Therefore, this threshold should be viewed not only as the minimum bulk water content required for DHMSs' appearance in the experimental system, but also as a petrologically meaningful boundary that determines whether subducted lithologies can effectively deliver water into the deeper mantle.

While previous studies[34,35] reported the coexistence of nominally anhydrous phases such as Wd and Rw with hydrous phases like Phase A and SuB, several experimental and mechanistic considerations suggest that this interpretation warrants cautious evaluation. First, the use of high surface-area starting materials (e.g., powders) in their experiments is likely to accelerate reaction kinetics, potentially leading to the rapid and complete consumption of free water through mineral reactions. This setup contrasts with natural systems, in which water incorporation into single-crystal structures is typically governed by slower, diffusion-limited processes. Despite considerable variations in initial H_2O contents among large olivine, Wd, and Rw single crystals, post-experiment analyses revealed a convergence toward similar final water concentrations. Hydrogen incorporation for metal vacancy diffusion in olivine results in an effective diffusion

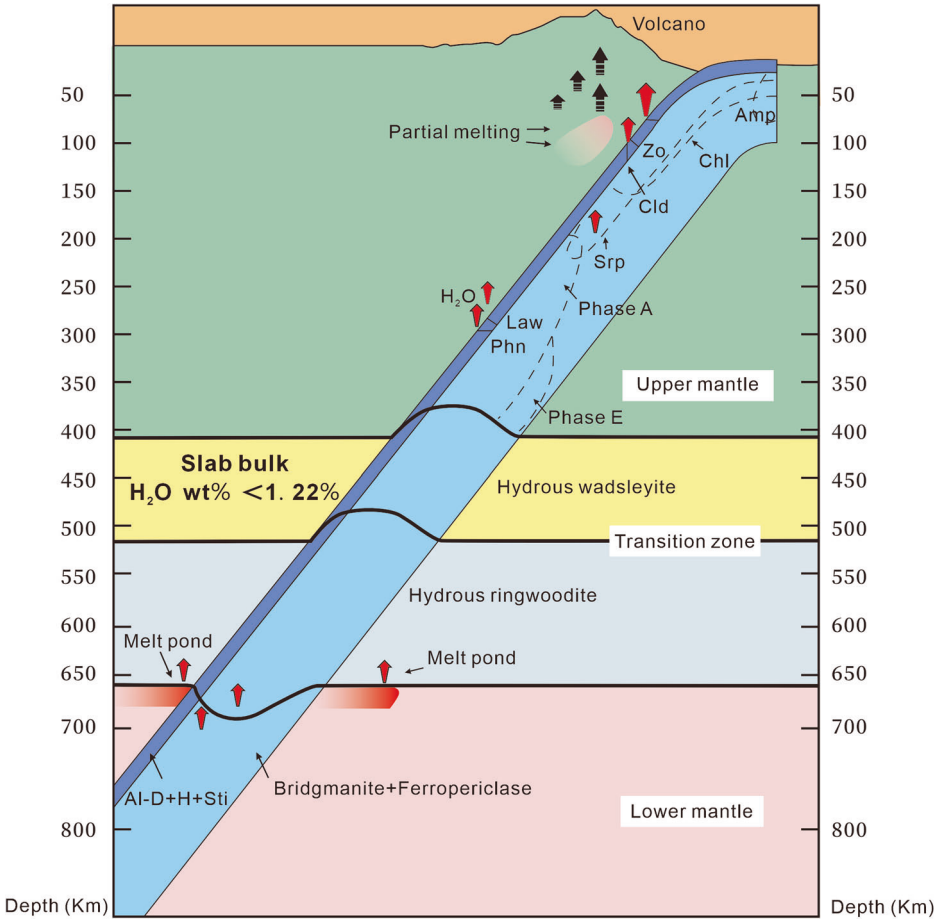

Fig. 3 | Modeled stability of hydrous phases in the descending slabs with H_2O content less than the critical point (1.22 wt%). Almost all minerals are completely dewatered at 300 km. Phase A could be the main water carrier to a depth of 400 km, with locally water-rich areas that may contain small amounts of phase E. In the mantle transition zone, water is mainly stored in hydrous wadsleyite and ringwoodite. At 660 km, ringwoodite decomposes, releasing water and forming hydrous melt layers. Only highly thermally stable phases, such as Al-rich phase D, phase H, and hydrous stishovite, could transport limited water into the lower mantle. Zo zoisite, Amp amphibole, Chl chlorite, Srp serpentine, Hy-Wd hydrous wadsleyite, Hy-Rw hydrous ringwoodite, Sti hydrous stishovite, Al-D Al-rich phase D, H phase H.

distance of only less than 0.2 μm, even after heating at 1173 K for 72 h[36] suggesting that after the experiment, the nominally anhydrous minerals are expected to remain almost the same as the initial amount of water. Considering the very slow kinetics at the temperature at which they carried out their experiments (1073 K), it is likely that wadsleyite remains as a non-equilibrium phase. In contrast, the matrix containing DHMSs surrounding the single crystals contains water far exceeding the threshold value, making it easy for hydrous minerals to form. This observation strongly supports the interpretation that H_2O distribution in these crystals is governed by hydrogen diffusion and equilibration with external a_{H_2O}, rather than by their initial hydration states or by chemical reactions. The tendency of both initially dry and wet olivine to approach a common H content indicates that the ambient a_{H_2O}, not mineral-bound capacity, dictates the final hydrogen inventory in olivine under the given experimental conditions[37]. Furthermore, even if phase transformations occurred, phase diagrams established in prior studies[8,25,38] indicate that the coexistence of SuB, Rw, and St, or of Phase A and En, is thermodynamically inconsistent with the known phase relations at the reported pressure–temperature conditions. Perhaps most critically, we can see from their results, particularly at 21 GPa, that the total water content of the matrix was 2.5 wt%. However, the water-bearing phase observed in the products is only SuB (grain size <1 μm) residing in the interstices of Rw crystals, and they assume Rw to be dry. Such a minute volume of SuB cannot possibly store up to 2.5 wt% water from the starting material, which falls far short of satisfying mass balance. Therefore, it is likely that the capsule was not completely sealed or that equilibrium was not achieved. In contrast, as shown in Fig. 1, our experiments demonstrate excellent agreement between observed results and calculated phase equilibria while water preferentially partitions into Wd and Rw rather than forming hydrous mineral phases, and they are consistent with previous studies conducted at high water contents. This convergence provides strong support for the achievement of equilibrium.

Water distribution in the subducted oceanic slab

It is widely accepted that hydrous minerals, e.g., serpentine, talc, and amphibole, are the principal water carriers for the subducted oceanic slab at the shallower upper mantle[39]. The extent to which these hydrous phases can transport water into the Earth's interior during subduction depends largely on pressure–temperature conditions. Most hydrous minerals will gradually dehydrate when the oceanic plate is subducted into about 660 km depth (Fig. 3). In the case of the hot slab, most hydrous minerals will dehydrate before they are subducted into the MTZ. The dehydrated water will be lost by upward migration due to its low density and wetting character ($\theta < 60°$) of both peridotite-water and basalt-water systems[17,40–44]. As for the cold slab, lower temperatures can stabilize hydrous minerals, such as serpentine, down to approximately 200 km depth, at which phase A serves as the main water carrier[6].

Upon reaching the MTZ, the ability of DHMSs to act as effective water carriers or not depends critically on the bulk water content of the subducting slab. Even in archetypal cold and water-rich systems such as the Mariana subduction zone, seismic observations indicate only limited slab hydration for a (24 ± 5) km thick, partially serpentinized slab mantle layer containing ~2 wt% water[15]. Once serpentine transforms into phase A at ~7 GPa, the mineral water content decreases from ~2 to ~0.8 wt%. Even under such deliberately chosen end-member scenarios representing extremely cold and hydrous subduction, the resulting bulk water contents remain well below the threshold required for the stabilization of DHMSs. Therefore, for the vast majority of subducting slabs, the bulk water content does not reach the level to stabilize DHMSs such as phase E, phase D, or superhydrous phase B. Furthermore, to stabilize these DHMSs phases to any notable degree, the

coexisting phase with olivine stoichiometry would have to be water-saturated, which is unlikely possible due to the lack of evidence for high V_p/V_s ratios[45] around active subduction zones within the MTZ[46,47].

In regions where the slab is locally enriched in water, the stability of DHMS may still be limited due to hydrogen chemical potential gradients between hydrous phases and adjacent, less hydrated assemblages. Whether the released water can be maintained in the subducted slab depends on the wetting behavior of the peridotite-water system and the overlying basalt-water system. According to the wetting behavior studies[17,42,44,48,49], the dihedral angles for fluid-Ol-Ol, fluid-Grt-Grt, fluid-Grt-Cpx, and fluid-Cpx-Cpx are all smaller than 60° at the 410 km boundary, indicating free water can migrate upwards freely driven by the density difference. This geometry facilitates efficient migration and loss of excess water through the oceanic crust, thereby preventing a large amount of water accumulation in the underlying peridotite. By reducing water activity through effective drainage, the water content in the peridotitic layer beneath the oceanic crust is expected to be well below that required for stabilization of DHMSs. This interpretation is supported by experimental observations, which demonstrate that hydrogen out-diffusion under relatively dry conditions can promote partial breakdown of DHMSs, even within nominally hydrous bulk environments[17,18]. Consequently, the amount of water transported into the MTZ by the subducted oceanic lithosphere is constrained to levels approaching the saturation of olivine, yielding undersaturated Wd and Rw. This conclusion is widely supported by studies, e.g., electrical conductivity[2], viscosity[3], rheology[5], mantle wedge dynamics[1], seismic activity[4].

As the slab subducts beyond the 660 km seismic discontinuity, hydrous Rw decomposes to bridgmanite, ferropericlase, and water. Due to the extremely low water solubility of bridgmanite and ferropericlase[50,51], the released water induces melt production at the 660 km discontinuity[52,53]. Hydrous melts are typically less dense than the surrounding mantle minerals and therefore tend to migrate upward[54,55]. However, under conditions of low-degree partial melting, the resulting melts can become enriched in Fe[56]. In this case, melts stabilize at the basement of the MTZ or migrate upward (depending on the melt composition and therefore the density difference). As a result, DHMSs cannot extensively form in the lower mantle to transport water deeper. However, in water-rich regions of subducting slabs, highly thermally stable hydrous phases such as phase H, Al-rich phase D, and Al-bearing post-stishovite may enable limited water transport into the lower mantle[10,13,57].

Conclusions

This study provides a deeper understanding of how water is stored and transported in the Earth's mantle, specifically within the MTZ. Our experiments revealed that the bulk water content of the subducted lithosphere strongly influences the stability of DHMSs. DHMSs only occur when the bulk water content exceeds a critical threshold of at least 1.22 wt% in the MTZ. Although there has been the traditional view that DHMSs are the main carriers of water into the deep mantle, the present study demonstrates that Wd and Rw are the principal water carriers in the MTZ rather than DHMSs, preventing substantial water transport into the lower mantle. Therefore, the large-scale water recycling may be restricted to depths shallower than around 660 km.

Methods

Starting materials and experimental details

The starting materials were mixtures of powders of synthetic forsterite (Mg_2SiO_4) and enstatite ($MgSiO_3$), and a regent of $Mg(OH)_2$. Forsterite was synthesized by solid-state reactions from stoichiometric mixtures of MgO and SiO_2 powders with molar ratios of 2:1. The mixtures were ground in an agate mortar, pelletized, and sintered at 1400 °C for 24 h. Enstatite was synthesized from MgO and SiO_2 powders mixed in a 1:1 molar ratio after calcination at 1273 K for 1 h. The mixture was ground to ~1 μm, loaded into a 0.02 mm thick Mo capsule, and held at 2 GPa and 1473 K for 20 h[58]. The ratios of these powders were set so that the bulk Mg/Si molar ratio was 1.4 according to the pyrolite model[59], and the H_2O contents were 0.1, 1, 1.6, 3, and 5 wt%. The powders were mixed and ground in an agate mortar for 2 h. The mixed powders were kept in an oven at 120 °C before being loaded into the gold capsule. The high-pressure experiments were carried out using a KAWAI-type multi-anvil apparatus installed at the Key Laboratory for High-Temperature and High-Pressure Study of the Earth's Interior, Institute of Geochemistry, Chinese Academy of Sciences, and 1000- and 5000-ton KAWAI-type multi-anvil presses installed with the Institute for Planetary Materials, Okayama University. The pressure medium was a Cr_2O_3-doped MgO octahedron with edge lengths of 14.0 and 8.0 mm, respectively, compressed by carbide anvils with truncated edge lengths of 6.0 and 3.0 mm to generate pressures of 16 (1) and 21.5 (10) GPa. The configurations of these high-pressure cell assemblies are shown schematically in Supplementary Fig. 1. A straight $LaCrO_3$ sleeve was used as the heater. Temperature was measured using a $W_{97}Re_3$–$W_{75}Re_{25}$ thermocouple. The sample was loaded into a gold capsule with an outer diameter of 1.0 mm and a length of 1.0–1.2 mm and sealed by welding. One and two capsules, respectively, were placed in the heater with MgO electrical insulation for runs at 21.5 and 16 GPa. The sample was compressed to the desired pressures and heated to 1400 K, followed by annealing at this temperature for 6, 12, or 24 h. The sample was then quenched by turning off the electrical power and recovered after 15 h of decompression.

Sample characterization

After recovery, microstructures and chemical compositions were analyzed using a field-emission scanning electron microscope (SEM) equipped with energy-dispersive X-ray spectroscopy (EDS) (Supplementary Fig. 2). For wadsleyite and phase E (phE), where Mg/Si ratios are close, it can indeed be challenging to distinguish between the two phases in a backscattered electron image under an SEM. This difficulty arises because Mg and Si have relatively close atomic numbers, leading to similar gray levels in BSE images, making phase differentiation challenging. Therefore, when BSE imaging fails to differentiate between phases with similar Mg/Si ratios, using EBSD can provide the necessary additional information to accurately distinguish these phases (Supplementary Fig. 3). The identification of phases was also accomplished through the utilization of a micro-focused X-ray diffractometer (Supplementary Figs. 4 and 5). The quantification of phase volume fractions within the recovered samples was conducted using the Image J software (Table 1).

A JSM-7800F Thermal Field Emission SEM, equipped with an EDS system, was employed for the semi-quantitative analysis of minerals. This study was conducted at the Key Laboratory for High-Temperature and High-Pressure Studies of the Earth's Interior, Institute of Geochemistry, Chinese Academy of Sciences. During the X-ray acquisition, a beam acceleration voltage of 15 kV with a 2 nA beam current was utilized. Beam size is less than 1 μm. For each phase identification of the run products, microfocus X-ray diffraction patterns were collected using a Brucker AXS D8 at Bayerisches Geoinstitut, University of Bayreuth. Discover a micro-focused XRD diffractometer, operating at 40 kV and 500 μA with CoKα radiation. Diffraction patterns were acquired over an exposure time of 3 h from an area of approximately ~100 μm^2. Phase identification was carried out using the PDindexer program[60]. EBSD was carried out by using a Zeiss Sigma 300VP FESEM and an Oxford Instruments Aztec Symmetry EBSD detector at the SEM-EBSD laboratory, School of Earth Sciences, China University of Geoscience, Wuhan. Working conditions were as follows: 20 kV accelerating voltage, 0.5μm spot size, working distance of 15 mm, 70° sample tilt angle, and low-vacuum mode of 20 Pa. Diffraction patterns were collected and indexed with an automatic mapping mode using the Aztec 6.1 software from Oxford Instruments. To assure data quality, only those measurements with mean angular deviation values below 1 degree were accepted for analyses.

The chemical compositions of the phases were analyzed using a JEOL JXA8200 electron probe microanalyzer, set at 15 kV and 5 nA to reduce electron beam damage to sensitive hydrous phases. The electron beam, approximately 1 μm in diameter, with peak counting times of 20 s, allowed for precise analysis. Si and Mg concentrations were determined using

diopside as standards. The detection limits for analysis are approximately 0.1 wt% for most elements. And the composition analysis uncertainty is less than 1 wt%.

Water content measurement

Secondary ion mass spectrometry (Nano-SIMS) analyses were performed using a CAMECA NanoSIMS 50L instrument at the State Key Laboratory of Ore Deposit Geochemistry, Chinese Academy of Sciences, Guiyang, China. Samples were polished and coated with a carbon layer approximately 40 nm thick to ensure conductivity under high voltage conditions. A mass resolution of about 7000 (M/ΔM measured at 10% peak height) was achieved by adjusting the width of the entrance slit (30 mm), exit slit (90 mm), and aperture slit (350 mm). This resolution was sufficient to eliminate isobaric interferences, including ^{17}O on $^{16}O^1H^-$, $^{29}Si^1H^-$ on $^{30}Si^-$, and $^{40}Ca^{--}$ on $^{24}Mg^{16}O^-$. The ions $^{16}O^-$, $^{16}O^1H^-$, $^{30}Si^-$, and $^{24}Mg^{16}O^-$ were detected simultaneously. The $^{16}O^-$ ion was measured using a Faraday cup detector, while the other ions ($^{16}O^1H^-$, $^{30}Si^-$, and $^{24}Mg^{16}O^-$) were detected by electron multiplier detectors.

Prior to each analysis[61], the sample surface was pre-sputtered for 50 s with a 50 pA primary beam over a $6 \times 6\ \mu m^2$ area to remove the carbon coating and to implant sufficient Cs^+ into the surface, thereby stabilizing secondary ion yields. During analysis, a primary Cs^+ ion beam of 50 pA was used, and the sampling area was $5 \times 5\ \mu m^2$.

To overcome matrix effects in Nano-SIMS analyses, a hydrous ringwoodite standard was synthesized. High-purity $Mg(OH)_2$ and SiO_2 powders (>99.9%) were used as starting materials. Prior to weighing, SiO_2 and $Mg(OH)_2$ powders were dried at 1370 and 400 K, respectively. The powders were mixed in ethanol to obtain a bulk composition corresponding to Mg_2SiO_4 plus 22 wt% H_2O. After drying in a vacuum furnace at 400 K to remove residual ethanol and moisture, the mixtures were sealed in Pt capsules (inner diameter 0.8 mm, outer diameter 1.0 mm) by arc welding. The capsule lengths were carefully controlled to ~1.2 mm after welding to minimize temperature gradients and uncertainties during high-pressure experiments. Each capsule was loaded into an MgO sleeve and placed within a $LaCrO_3$ furnace. A Cr_2O_3-doped MgO octahedron with an edge length of 7 mm served as the pressure medium. Temperature was monitored using a D-type thermocouple ($W_{97}Re_3$–$W_{75}Re_{25}$). The assemblies were compressed to 20 GPa at ambient temperature using a Kawai-type multi-anvil apparatus and subsequently heated to 1800 K at a rate of ~100 K/min. The samples were annealed at the target temperature for 240 min before quenching. The samples recovered were cut into two halves. One half was double-sided polished to a thickness of 50 μm for FTIR analysis to determine the H_2O content, while the other half was used as a NanoSIMS standard. FTIR spectra are shown in Supplementary Fig. 6, and the baseline correction and the method for calculating water content followed the procedure described by Fei and Katsura (2020). The hydrous ringwoodite standard sample contains 2.11(2) wt% H_2O.

Data availability

The data supporting the findings of this study are provided in the Supplementary Information. These data are also available via Zenodo at https://doi.org/10.5281/zenodo.18765147 (ref. 62).

Received: 11 September 2025; Accepted: 26 February 2026;
Published online: 25 March 2026

References

1. Arcay, D., Tric, E. & Doin, M.-P. Numerical simulations of subduction zones. *Phys. Earth Planet. Inter.* **149**, 133–153 (2005).
2. Yoshino, T., Manthilake, G., Matsuzaki, T. & Katsura, T. Dry mantle transition zone inferred from the conductivity of wadsleyite and ringwoodite. *Nature* **451**, 326–329 (2008).
3. Nakao, A., Iwamori, H. & Nakakuki, T. Effects of water transportation on subduction dynamics: roles of viscosity and density reduction. *Earth Planet. Sci. Lett.* **454**, 178–191 (2016).
4. Ferrand, T. P. et al. Dehydration-driven stress transfer triggers intermediate-depth earthquakes. *Nat. Commun*. **8**, 15247 (2017).
5. Behr, W. M., Kotowski, A. J. & Ashley, K. T. Dehydration-induced rheological heterogeneity and the deep tremor source in warm subduction zones. *Geology* **46**, 475–478 (2018).
6. Ulmer, P. & Trommsdorff, V. Serpentine stability to mantle depths and subduction-related magmatism. *Science* **268**, 858–861 (1995).
7. Komabayashi, T. & Omori, S. Internally consistent thermodynamic data set for dense hydrous magnesium silicates up to 35 GPa, 1600 °C: implications for water circulation in the Earth's deep mantle. *Phys. Earth Planet. Inter.* **156**, 89–107 (2006).
8. Komabayashi, T., Omori, S. & Maruyama, S. Experimental and theoretical study of stability of dense hydrous magnesium silicates in the deep upper mantle. *Phys. Earth Planet. Inter.* **153**, 191–209 (2005).
9. Tsuchiya, J. First principles prediction of a new high-pressure phase of dense hydrous magnesium silicates in the lower mantle. *Geophys. Res. Lett.* **40**, 4570–4573 (2013).
10. Nishi, M. et al. Stability of hydrous silicate at high pressures and water transport to the deep lower mantle. *Nat. Geosci.* **7**, 224–227 (2014).
11. Ohira, I. et al. Stability of a hydrous δ-phase, AlOOH–$MgSiO_2(OH)_2$, and a mechanism for water transport into the base of lower mantle. *Earth Planet. Sci. Lett.* **401**, 12–17 (2014).
12. Ono, S. Stability limits of hydrous minerals in sediment and mid-ocean ridge basalt compositions: implications for water transport in subduction zones. *J. Geophys. Res. Solid Earth* **103**, 18253–18267 (1998).
13. Ishii, T. et al. Superhydrous aluminous silica phases as major water hosts in high-temperature lower mantle. *Proc. Natl. Acad. Sci. USA*. **119**, e2211243119 (2022).
14. Yu, Y. et al. Unraveling the complex features of the seismic scatterers in the mid-lower mantle through phase transition of (Al, H)-bearing stishovite. *Geophys. Res. Lett.* **52**, e2024GL114146 (2025).
15. Cai, C., Wiens, D. A., Shen, W. & Eimer, M. Water input into the Mariana subduction zone estimated from ocean-bottom seismic data. *Nature* **563**, 389–392 (2018).
16. Schmidt, M. W. & Poli, S. Experimentally based water budgets for dehydrating slabs and consequences for arc magma generation. *Earth Planet. Sci. Lett.* **163**, 361–379 (1998).
17. Guo, X., Yoshino, T., Chen, S., Wu, X. & Zhang, J. Partial dehydration of brucite and its implications for water distribution in the subducting oceanic slab. *Geosci. Front.* **13**, 101342 (2022).
18. Guo, X. & Yoshino, T. Electrical conductivity of dense hydrous magnesium silicates with implication for conductivity in the stagnant slab. *Earth Planet. Sci. Lett.* **369–370**, 239–247 (2013).
19. Kohlstedt, D. L., Keppler, H. & Rubie, D. C. Solubility of water in the α, β and γ phases of $(Mg,Fe)_2SiO_4$. Contrib. Mineral. Petrol. **123**, 345–357 (1996).
20. Inoue, T., Yurimoto, H. & Kudoh, Y. Hydrous modified spinel, $Mg_{1.75}SiH_{0.5}O_4$: a new water reservoir in the mantle transition region. *Geophys. Res. Lett.* **22**, 117–120 (1995).
21. Pearson, D. G. et al. Hydrous mantle transition zone indicated by ringwoodite included within diamond. *Nature* **507**, 221–224 (2014).
22. Fei, H. & Katsura, T. High water solubility of ringwoodite at mantle transition zone temperature. *Earth Planet. Sci. Lett.* **531**, 115987 (2020).
23. Fei, H. & Katsura, T. Water solubility in Fe-bearing wadsleyite at mantle transition zone temperatures. *Geophys. Res. Lett.* **48**, e2021GL092836 (2021).
24. Angel, R. J., Frost, D. J., Ross, N. L. & Hemley, R. Stabilities and equations of state of dense hydrous magnesium silicates. *Phys. Earth Planet. Inter.* **127**, 181–196 (2001).
25. Ohtani, E., Mizobata, H. & Yurimoto, H. Stability of dense hydrous magnesium silicate phases in the systems Mg_2SiO_4-H_2O and $MgSiO_3$-H_2O at pressures up to 27 GPa. *Phys. Chem. Miner.* **27**, 533–544 (2000).

26. Litasov, K. & Ohtani, E. Stability of various hydrous phases in CMAS pyrolite-H_2O system up to 25 GPa. *Phys. Chem. Miner.* **30**, 147–156 (2003).
27. Bolfan-Casanova, N. Water partitioning between nominally anhydrous minerals in the MgO–SiO_2–H_2O system up to 24 GPa: implications for the distribution of water in the Earth's mantle. *Earth Planet. Sci. Lett.* **182**, 209–221 (2000).
28. Purevjav, N. et al. Temperature dependence of H_2O solubility in Al-free stishovite. *Geophys. Res. Lett*. **51**, e2023GL104029 (2024).
29. Yang, X., Liu, D. & Xia, Q. CO_2-induced small water solubility in olivine and implications for properties of the shallow mantle. *Earth Planet. Sci. Lett.* **403**, 37–47 (2014).
30. Guo, X., Bai, J., Wang, C., Wu, X. & Zhou, X. CO_2 induced a small water solubility in orthopyroxene and its implications for water storage in the upper mantle. *J. Geophys. Res. Solid Earth* **125**, e2019JB018745 (2020).
31. Frost, D. J. & McCammon, C. A. The redox state of Earth's mantle. *Annu. Rev. Earth Planet. Sci.* **36**, 389–420 (2008).
32. Duan, Z. & Zhang, Z. Equation of state of the H_2O, CO_2, and H_2O–CO_2 systems up to 10 GPa and 2573.15K: molecular dynamics simulations with ab initio potential surface. *Geochim. Cosmochim. Acta* **70**, 2311–2324 (2006).
33. Manning, C. The chemistry of subduction-zone fluids. *Earth Planet. Sci. Lett.* **223**, 1–16 (2004).
34. Ishii, T. & Ohtani, E. Dry metastable olivine and slab deformation in a wet subducting slab. *Nat. Geosci.* **14**, 526–530 (2021).
35. Ishii, T., Zhu, J. & Ohtani, E. Limited water contents of wadsleyite and ringwoodite coexisting with hydrous minerals in cold subducting slabs. *Earth Planet. Sci. Lett.* **658**, 119310 (2025).
36. Demouchy, S. & Mackwell, S. Mechanisms of hydrogen incorporation and diffusion in iron-bearing olivine. *Phys. Chem. Miner.* **33**, 347–355 (2006).
37. Sarafian, E., Gaetani, G. A., Hauri, E. H. & Sarafian, A. R. Experimental constraints on the damp peridotite solidus and oceanic mantle potential temperature. *Science* **355**, 942–945 (2017).
38. Ono, S., Kikegawa, T. & Higo, Y. Reaction boundary between akimotoite and ringwoodite + stishovite in $MgSiO_3$. *Phys. Chem. Miner.* **44**, 425–430 (2017).
39. Ohtani, E. & Ishii, T. Role of water in dynamics of slabs and surrounding mantle. *Prog. Earth Planet. Sci.* **11**, 65 (2024).
40. Ono, S., Mibe, K. & Yoshino, T. Aqueous fuid connectivity in pyrope aggregates: water transport into the deep mantle by a subducted oceanic crust without any hydrous minerals. Earth Planet. Sci. Lett. **203**, 895–903 (2002).
41. Mibe, K., Yoshino, T., Ono, S., Yasuda, A. & Fujii, T. Connectivity of aqueous fluid in eclogite and its implications for fluid migration in the Earth's interior. *J. Geophys. Res. Solid Earth* **108**, https://doi.org/10.1029/2001GL014457 (2003).
42. Yoshino, T., Nishihara, Y. & Karato, S. Complete wetting of olivine grain boundaries by a hydrous melt near the mantle transition zone. *Earth Planet. Sci. Lett.* **256**, 466–472 (2007).
43. Matsukage, K. N., Hashimoto, M. & Nishihara, Y. Morphological stability of hydrous liquid droplets at grain boundaries of eclogite minerals in the deep upper mantle. *J. Mineral. Petrol. Sci.* **112**, 346–358 (2017).
44. Liu, X. et al. Aqueous fluid connectivity in subducting oceanic crust at the mantle transition zone conditions. *J. Geophys. Res. Solid Earth* **123**, 6562–6573 (2018).
45. Chen, W.-P. & Brudzinski, M. R. Evidence for a large-scale remnant of subducted lithosphere beneath Fiji. *Science* **292**, 2475–2479 (2001).
46. Green, H. W. Shearing instabilities accompanying high-pressure phase transformations and the mechanics of deep earthquakes. *Proc. Natl. Acad. Sci. USA*. **104**, 9133–9138 (2007).
47. Green Ii, H. W., Chen, W.-P. & Brudzinski, M. R. Seismic evidence of negligible water carried below 400-km depth in subducting lithosphere. *Nature* **467**, 828–831 (2010).
48. Mibe, K., Fujii, T. & Yasuda, A. Control of the location of the volcanic front in island arcs by aqueous Øuid connectivity in the mantle wedge. *Nature* **401**, 259–262 (1999).
49. Mibe, K., Fujii, T. & Yasuda, A. Connectivity of aqueous fluid in the Earth's upper mantle. *Geophys. Res. Lett.* **25**, 1233–1236 (1998).
50. Liu, Z. et al. Bridgmanite is nearly dry at the top of the lower mantle. *Earth Planet. Sci. Lett.* **570**, 117088 (2021).
51. Bolfan-Casanova, N., Mackwell, S., Keppler, H., McCammon, C. & Rubie, D. C. Pressure dependence of H solubility in magnesiowüstite up to 25 GPa: implications for the storage of water in the Earth's lower mantle. *Geophys. Res. Lett*. **29**, https://doi.org/10.1029/2001GL014457 (2002).
52. Schmandt, B. & Steven, J. Dehydration melting at the top of the lower mantle. *Science* **344**, 1265–1268 (2014).
53. Nakajima, A., Sakamaki, T., Kawazoe, T. & Suzuki, A. Hydrous magnesium-rich magma genesis at the top of the lower mantle. *Sci. Rep*. **9**, 7420 (2019).
54. Fei, H. Water content of the dehydration melting layer in the topmost lower mantle. *Geophys. Res. Lett*. **48**, e2020GL090973 (2021).
55. Fei, H. Stability of H_2O-rich fluid in the deep mantle indicated by the MgO-SiO_2-H_2O phase relations at 23 GPa and 2000 K. *J. Geophys. Res. Solid Earth* **129**, e2024JB029446 (2024).
56. Kuwahara, H. Partial melt composition of enstatite chondritic mantle around the rheological transition at 23 GPa: implications for the chemical differentiation of the Earth's mantle. *Phys. Earth Planet. Inter.* **346**, 107123 (2024).
57. Pamato, M. G. et al. Lower-mantle water reservoir implied by the extreme stability of a hydrous aluminosilicate. *Nat. Geosci.* **8**, 75–79 (2015).
58. Feng, B. & Guo, X. Thermal conductivity and thermal diffusivity of ferrosilite under high temperature and high pressure. *J. Earth Sci.* **33**, 770–777 (2022).
59. McDonough, W. F. & Sun, S.-s. The composition of the Earth. *Chem. Geol*. **120**, 223–253 (1995).
60. Seto, Y., Nishio-Hamane, D., Nagai, T. & Sata, N. Development of a software suite on X-ray diffraction experiments. *Rev. High Press. Sci. Technol.* **20**, 269–276 (2010).
61. Chen, Y. A quantity chalcopyrite reference material for in situ sulfur isotope analysis. *At. Spectrosc.* **44**, 131–141 (2023).
62. Song Y. & Guo, X. Stability and distribution of dense hydrous magnesium silicates in the mantle transition zone under low water activity conditions. Zenodo, https://doi.org/10.5281/zenodo.18765147 (2026).

Acknowledgements

The authors would like to thank Guoliang Niu, Shuangmeng Zhai, Weihong Xue, Hongzhan Fei, and Tomoo Katsura for their helpful discussions. The authors appreciate the financial support of the National Natural Science Foundation of China (No. 42072051 and 42572039), Guizhou Provincial 2021 Science and Technology Subsidies (GZ2021SIG), the CAS "Light of West China" program (Y9CR026 to X.G.), and the Chinese Scholarship Council (CSC, No. 202304910412 to Y.S.).

Author contributions

Conceptualization: Y.S. and X.G. Methodology: Y.S., W.G., K.Z., and X.G. Investigation: Y.S. and X.G. Visualization: Y.S., K.Z., and X.G. Funding acquisition: X.G. Project administration: X.G. Supervision: X.G. and T.Y. Writing original draft: Y.S., X.G., and T.Y. Writing—review and editing: all authors.

Competing interests

The authors declare no competing interests.

Additional information

Supplementary information The online version contains supplementary material available at https://doi.org/10.1038/s43247-026-03379-1.

Correspondence and requests for materials should be addressed to Xinzhuan Guo.

Peer review information *Communications Earth & Environment* thanks the anonymous reviewers for their contribution to the peer review of this work. Primary Handling Editors: Renbiao Tao and Alireza Bahadori. A peer review file is available.